JACS Au
AN OPEN ACCESS JOURNAL OF THE AMERICAN CHEMICAL SOCIETY

pubs.acs.org/jacsau

Article

Onset of High Methane Combustion Rates over Supported Palladium Catalysts: From Isolated Pd Cations to PdO Nanoparticles

Yanran Cui, Johnny Zhu Chen, Bo Peng, Libor Kovarik, Arun Devaraj, Zhe Li, Tao Ma, Yilin Wang, Janos Szanyi, Jeffrey T. Miller, Yong Wang,* and Feng Gao*

Cite This: *JACS Au* 2021, 1, 396–408

Read Online

ACCESS | Metrics & More | Article Recommendations | Supporting Information

ABSTRACT: Industrial low-temperature methane combustion catalyst Pd/Al_2O_3 suffers from H_2O-induced deactivation. It is imperative to design Pd catalysts free from this deactivation and with high atomic efficiency. Using a small-pore zeolite SSZ-13 as support, herein we report well-defined Pd catalysts with dominant active species as finely dispersed Pd cations, uniform PdO particles embedded inside the zeolite framework, or PdO particles decorating the zeolite external surface. Through detailed reaction kinetics and spectroscopic and microscopic studies, we show that finely dispersed sites are much less active than PdO nanoparticles. We further demonstrate that H_2O-induced deactivation can be readily circumvented by using zeolite supports with high Si/Al ratios. Finally, we provide a few rational catalyst design suggestions for methane oxidation based on the new knowledge learned in this study.

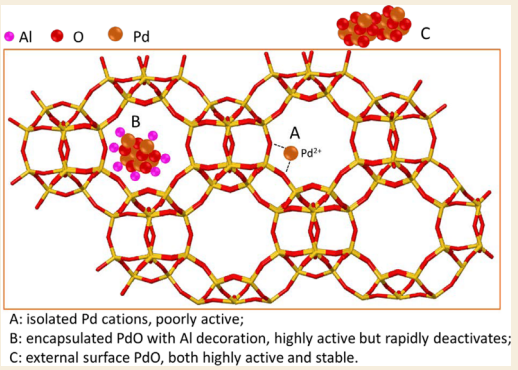

A: isolated Pd cations, poorly active;
B: encapsulated PdO with Al decoration, highly active but rapidly deactivates;
C: external surface PdO, both highly active and stable.

KEYWORDS: *catalytic methane combustion, palladium catalyst, zeolite catalyst, reaction kinetics, emission pollution abatement*

INTRODUCTION

Catalytic methane combustion to CO_2 and H_2O owns considerable practical importance, e.g., in energy generation and in reducing the release of this greenhouse gas into the atmosphere.[1−3] Fundamentally, it is also an interesting model catalytic reaction as it can be catalyzed by active sites of varying nature and reaction mechanisms.[4] Over supported Pd, studies by Chin et al.[5] demonstrated that with increasing oxygen content of the catalysts, active sites for C−H activation evolve from metal atom pairs (*−*) to chemisorbed oxygen atom (O*−O*) pairs and ultimately to Pd cation-lattice oxygen pairs (Pd^{2+}−O^{2-}) in PdO, where the transition state on PdO is much more stable than those on *−* and O*−O* pairs, giving rise to a large increase in CH_4 oxidation turnover rates at oxygen chemical potentials leading to Pd to PdO transitions. The Pd to PdO transition, however, can encounter kinetic hurdles for two reasons: (1) difficulty for oxygen diffusion into metallic Pd at low temperatures and (2) formation of a strongly bound oxygen passivation layer at high temperatures.[3] Such hurdles explain the "hysteresis" behavior in methane combustion, i.e., activity loss by delayed Pd oxidation to PdO.[6,7] However, the frequently encountered transient phases under nonsteady-state operations are still not fully understood, and the nature of the most active Pd phases under such operations are still debated.[8−10] This is further complicated by the lack of understanding of the Pd phase nuclearity and support effects, although previous studies reported weak PdO particle size and support effects (i.e., structure insensitivity) under reaction conditions where PdO is generally agreed to be the active phase, i.e., high O_2/CH_4 ratios and relatively low temperatures.[11,12]

Pd supported on alumina (Pd/Al_2O_3) is generally regarded as the "standard" catalyst for the conversion of unburned methane from (compressed natural gas) engine exhausts.[13] Unfortunately, Pd/Al_2O_3 severely deactivates during low-temperature methane combustion in the presence of water vapor.[14] Likely causes include (1) gradual hydroxylation of active PdO to less active $Pd(OH)_2$[14] or (2) hydroxylation of the Al_2O_3 support, which slows active lattice oxygen replenishment.[15,16] The current industrial solution in avoiding deactivation is to add platinum to the catalyst.[17−20] Pt introduction slows PdO sintering and enables the formation of Pt−Pd bimetallic phases that are not readily hydroxylated by water vapor. However, the catalyst stability enhancement benefited from this practice is compromised by catalyst activity loss; Pt−Pd bimetallic phases are much less active than PdO under the low-temperature, oxygen-rich reaction conditions.[18,21]

Received: December 13, 2020
Published: March 25, 2021

https://doi.org/10.1021/jacsau.0c00109
JACS Au 2021, 1, 396−408

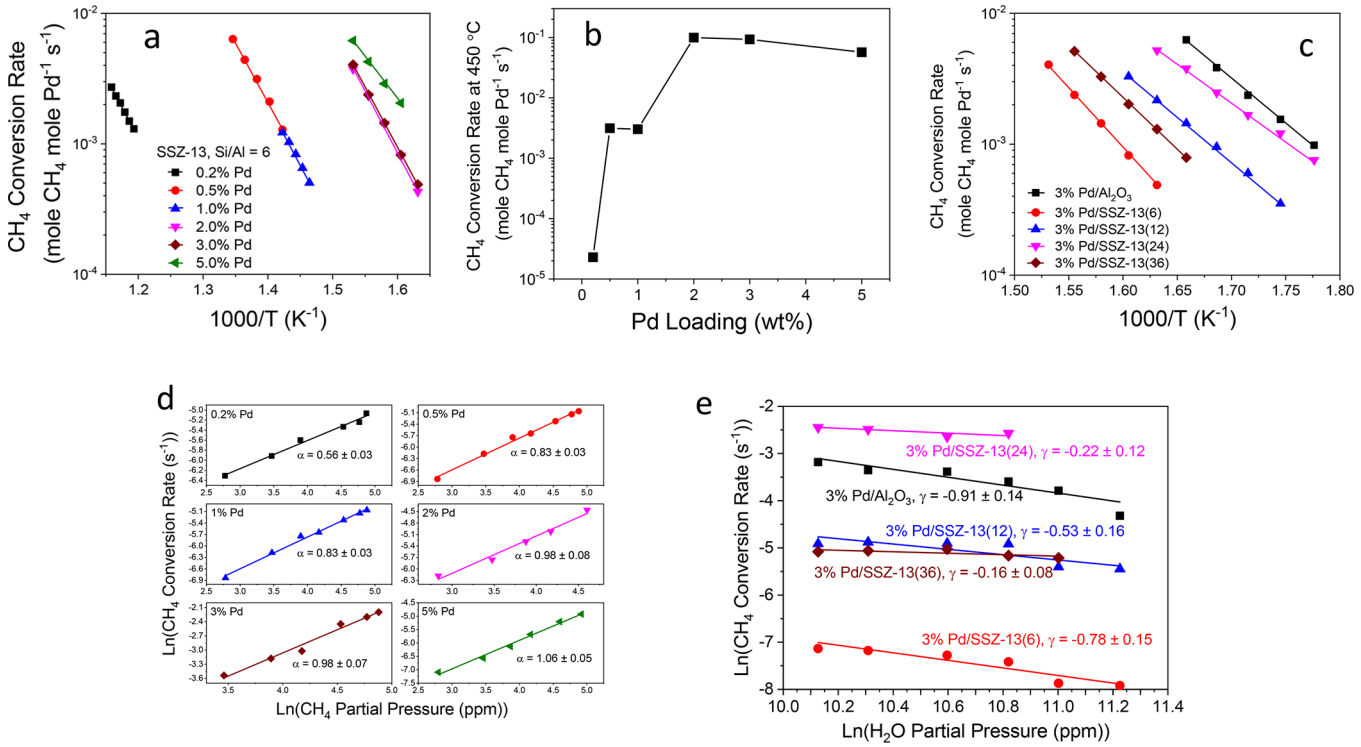

Figure 1. Low-temperature methane combustion kinetics results. (a) Normalized reaction rates (mole CH_4 mole Pd^{-1} s^{-1}) in the form of Arrhenius plots over Pd/SSZ-13(6) catalysts with varying Pd loadings. Reactant feed composition: CH_4 640 ppm, 14% O_2, 5% CO_2, and 2.5% H_2O, balanced with N_2. Total flow is 300 mL/min. Catalysts were diluted with inert SiO_2 with catalyst-to-SiO_2 ratios as follows: 0.2−1% Pd (1:1); 2% Pd (1:3); 3−5% Pd (1:9). 120 mg of diluted catalyst was used for each experiment. (b) Reaction rates at 450 °C as a function of Pd loading. (c) Arrhenius plots for the 3% Pd/SSZ-13 catalysts with varying support Si/Al ratios and a reference 3% Pd/Al_2O_3 catalyst. Catalysts were diluted with inert SiO_2 with a catalyst-to-SiO_2 ratio of 1:9. 120 mg of diluted catalyst was used for each experiment. (d) CH_4 pressure dependence plots over Pd/SSZ-13(6) catalysts with varying Pd loadings. Reactant feed compositions: CH_4 pressures varying from ∼200 to ∼1000 ppm, 14% O_2, 5% CO_2, and 2.5% H_2O, balanced with N_2. Total flow is 300 mL/min. 120 mg of diluted catalyst was used for each experiment. Catalyst dilution and reaction temperature conditions are as follows: 0.2−1% Pd, 1:1 dilution, 420 °C; 2% Pd, 1:4 dilution, 380 °C; 3% Pd 1:199 dilution, 480 °C; 5% Pd, 1:9 dilution, 360 °C. (e) H_2O pressure dependence plots over 3% Pd/SSZ-13 catalysts with varying support Si/Al ratios and the 3% Pd/Al_2O_3 catalyst. Reactant feed compositions: 640 ppm of CH_4, 14% O_2, 5% CO_2, H_2O pressures varying from ∼1.0 to ∼7.5%, balanced with N_2. Total flow is 300 mL/min. 120 mg of (diluted) catalyst was used for each measurement. The catalyst dilution conditions and reaction temperatures are as follows: (1) 3% Pd/Al_2O_3, 1:199 dilution, 400 °C; (2) 3% Pd/SSZ-13(6), 1:9 dilution, 385 °C; (3) 3% Pd/SSZ-13(12), 1:3 dilution, 380 °C; (4) 3% Pd/SSZ-13(24), 1:199 dilution, 370 °C; (5) 3% Pd/SSZ-13(36), 1:9 dilution, 365 °C.

The current grand challenges in designing new low-temperature methane combustion catalysts are 2-fold: (1) light-off temperatures lower than ∼300 °C and (2) resistance to water vapor. From recent literature, catalysts with high initial rates for "dry" methane combustion have frequently been reported.[1,22−24] However, such improved performance is seldom sustained in the presence of water vapor. Herein, we report low-temperature methane combustion over small-pore zeolite SSZ-13 supported Pd (Pd/SSZ-13) catalysts. To our knowledge, there have been two recent open literature studies using the same catalyst for methane combustion.[25,26] These studies focus mainly on catalyst performance and stability. To obtain more in-depth molecular-level knowledge on the nature of the active species, reaction mechanisms, and structure−function correlations, herein by controlling Pd loading and support Si/Al ratio, we show that Pd dispersion and location can be well-controlled, allowing us to probe activities for finely dispersed Pd^{2+} cations, PdO nanoparticles embedded inside zeolite particles, and PdO nanoparticles decorating the zeolite external surface, all in the presence of water vapor. Reaction kinetics studies demonstrate that finely dispersed sites are substantially less active than PdO nanoparticles. We further demonstrate that water vapor-induced catalyst deactivation can be greatly suppressed by eliminating PdO-Al_2O_3 interactions. These new findings provide important guidelines for designing highly active, robust methane combustion catalysts for emission control applications.

RESULTS AND DISCUSSION

Methane Combustion Kinetics

Figure 1a presents Arrhenius plots for the Pd/SSZ-13(6) catalysts with varying Pd loadings from 0.2 to 5 wt % (steady-state differential rates are normalized to total Pd contents; "(6)" denotes the Si/Al ratio of the support). Using the reaction data, apparent activation energies are readily calculated, and the values are tabulated in Table 1. It is worthwhile noting that all samples display apparent activation energies of ∼180 kJ/mol except the 5% Pd/SSZ-13(6), which shows a much lower apparent activation energy of 124 kJ/mol. A marked reaction rate dependence on Pd loading is evident. Using rates either measured or extrapolated using the Arrhenius equation and the corresponding apparent activation energies, Figure 1b plots rates at 450 °C as a function of Pd loading. As the Pd content increases from 0.2 to 0.5−1%, CH_4 conversion rates increase by 2 orders of magnitude; by further

https://doi.org/10.1021/jacsau.0c00109
JACS Au 2021, 1, 396−408

Table 1. Surface Area/Porosity, Pd Content, PdO Content, CH_4 Combustion Apparent Activation Energy, and Reaction Order Dependences on $CH_4/O_2/H_2O/CO_2$ Pressures

						CH_4 combustion pressure dependence			
catalyst	BET surface area (m^2/g)	pore volume (cm^3/g)	Pd content by ICP (wt %)	Pd as PdO by TPD (wt %)	CH_4 combustion E_a (kJ mol^{-1})	CH_4	O_2	H_2O	CO_2
0.2% Pd/SSZ-13 (6)	583	0.32	0.18	n.d.	177.5 ± 2.8	0.56 ± 0.03	0.23 ± 0.02	−0.34 ± 0.07	−0.05 ± 0.08
0.5% Pd/SSZ-13 (6)	557	0.31	0.48	n.d.	171.2 ± 5.9	0.83 ± 0.03	0.05 ± 0.03	−0.43 ± 0.09	0.01 ± 0.03
1% Pd/SSZ-13 (6)	564	0.31	1.0	$\sim 6.4 \times 10^{-3}$	178.5 ± 7.4	0.83 ± 0.03	0.10 ± 0.01	−0.68 ± 0.19	0.07 ± 0.02
2% Pd/SSZ-13 (6)	580	0.32	1.93	0.23	179.2 ± 4.7	0.98 ± 0.08	0.05 ± 0.01	−0.88 ± 0.17	0.01 ± 0.02
3% Pd/SSZ-13 (6)	568	0.31	2.74	0.32	176.1 ± 2.0	0.98 ± 0.07	0.08 ± 0.06	−0.78 ± 0.15	−0.04 ± 0.05
5% Pd/SSZ-13 (6)	555	0.31	5.26	1.66	124.7 ± 3.2	1.06 ± 0.05	0.01 ± 0.04	−0.81 ± 0.24	0.01 ± 0.01
3% Pd/Al_2O_3	76	0.38	2.60	2.60	130.1 ± 3.5	0.99 ± 0.04	0.01 ± 0.03	−0.91 ± 0.14	0.02 ± 0.03
3% Pd/SSZ-13 (12)	587	0.32	2.10	1.64	131.0 ± 2.0	0.94 ± 0.03	0.03 ± 0.01	−0.53 ± 0.16	0.01 ± 0.02
3% Pd/SSZ-13 (24)	553	0.31	2.31	2.28	119.1 ± 2.3	1.04 ± 0.07	0.07 ± 0.02	−0.22 ± 0.12	−0.02 ± 0.01
3% Pd/SSZ-13 (36)	331	0.18	2.82	2.75	117.3 ± 2.6	1.04 ± 0.07	0.09 ± 0.01	−0.16 ± 0.08	0.03 ± 0.03

increasing Pd loading to 2−5%, CH_4 conversion rates increase by 4 orders of magnitude compared to that of 0.2% Pd. Figure 1c depicts comparative Arrhenius plots for 3% Pd/SSZ-13 catalysts with Si/Al ratios from 6 to 36 and a reference 3% Pd/Al_2O_3 sample. In this case, all Pd/SSZ-13 samples appear to be less active than Pd/Al_2O_3, with normalized rates lowered by as much as 1 order of magnitude; the rates for the Pd/SSZ-13 samples do not appear to have a clear trend as a function of the support Si/Al ratio. Regarding apparent activation energies, all zeolite supported ones, except 3% Pd/SSZ-13(6), show similar values as that of Pd/Al_2O_3.

The empirical power-law rate expression $r_{CH_4} = kp^{\alpha}_{CH_4}p^{\beta}_{O_2}p^{\gamma}_{H_2O}p^{\delta}_{CO_2}$ was further applied to obtain pressure orders on reactants CH_4 and O_2 and products H_2O and CO_2. The plots are detailed in the Supporting Information Figures S1−S6, and the pressure order values are summarized in Table 1. Overall, the measured orders are consistent with literature reports for supported Pd catalysts: methane displays positive orders consistent with its low-sticking nature; H_2O displays negative powers due to its inhibiting effect, and O_2 and CO_2 display near-zero order dependences.[3,4,27,28] Two important trends are observed here. First, as shown in Figure 1d, the series of Pd/SSZ-13(6) catalysts display a clear trend on methane pressure orders: the 0.2% Pd loaded sample shows a surprisingly low order of 0.56, which increases to ∼1.0 as Pd loadings become 0.5% and above. This may suggest that the nature of active Pd species in the 0.2% Pd sample is distinct from others. Second, from Figure 1e presenting H_2O pressure orders for the series of 3% Pd catalysts, the Pd/Al_2O_3 catalyst shows an expected H_2O order of −0.91 consistent with literature.[27−29] But interestingly, as the Si/Al ratio of the Pd/SSZ-13 catalysts increases, the H_2O order gradually changes from ∼−0.8 to ∼−0.2, i.e., water vapor inhibition to the reaction gradually weakens as the support Si/Al ratio increases. We also note that there exists an interesting correlation between support Si/Al ratio and catalyst deactivation, where increased support Si/Al ratio leads to much improved catalyst stability. Such data are presented in Figures S7−S10.

Pd Location and Dispersion

The kinetics data shown above suggest the presence of different types of Pd species with distinct activities toward methane combustion. We have recently shown in our studies on zeolite supported Pd passive NOx adsorber (PNA) materials that Si/Al ratio plays a decisive role in determining Pd location and dispersion.[30,31] On SSZ-13 supports with low Si/Al ratios, Pd tends to migrate inside the zeolite particle and stay highly dispersed. As the support Si/Al ratio increases, Pd largely remains on the external surfaces. It can be suggested, then, that finely dispersed Pd species are much less active than PdO (the active phase on Pd/Al_2O_3) in catalyzing methane oxidation. For zeolite supported catalysts that display similar kinetic behavior as Pd/Al_2O_3, it is likely that PdO is also the active phase in them. Next, via high angle annular dark field scanning transmission electron microscopy (HAADF-STEM), powder X-ray diffraction (XRD), and atom probe tomography (APT), we demonstrate the remarkable influences of Pd loading and Si/Al ratio to Pd nuclearity and location. Prior to such measurements, the samples were stabilized under methane combustion reaction conditions at 400 °C for ∼20 h in the presence of 2.5% H_2O.

From the upper panel images of Figure 2, lattice fringes of the SSZ-13(6) support are readily observed for samples with Pd loadings of 0.2% and 1% (Figure 2a, b); features that may be attributable to Pd single atoms or clusters are not seen, consistent with the atomically dispersed ionic nature for the predominant Pd sites in these samples.[30,31] As the Pd loading increases to 2% and above, uniform bright features measuring 2.5 ± 1.5 nm are imaged; these are readily attributed to PdO particles. The precise locations of these particles, i.e., whether these are encapsulated within the zeolite particles, or they stay at external surfaces, cannot be readily determined by such images alone. It can be suggested, however, that encapsulated particles tend to have more uniform particle sizes because of

https://doi.org/10.1021/jacsau.0c00109
JACS Au 2021, 1, 396−408

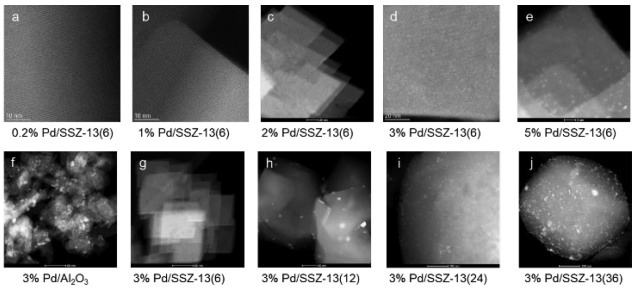

Figure 2. HAADF-STEM images for the catalysts. (a) 0.2% Pd/SSZ-13(6). (b) 1% Pd/SSZ-13(6). (c) 2% Pd/SSZ-13(6). (d) 3% Pd/SSZ-13(6). (e): 5% Pd/SSZ-13(6). (f): 3% Pd/Al_2O_3. (g): 3% Pd/SSZ-13(6). (h): 0.2% Pd/SSZ-13(12). (i): 3% Pd/SSZ-13(24). (j): 3% Pd/SSZ-13(36). Before imaging, all catalysts were stabilized under wet (2.5% H_2O) methane combustion conditions for ~20 h at ~400 °C.

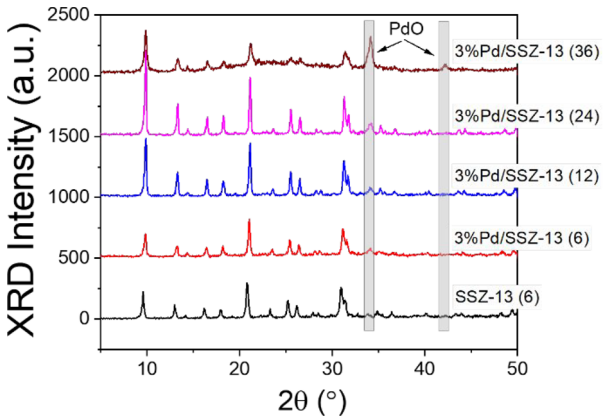

Figure 3. XRD patterns for SSZ-13(6) and 3% Pd/SSZ-13 catalysts with different Si/Al ratios. Data were collected with 2θ ranging from 5 to 50° using a step size of 0.02°. PdO reflections at 34.1 and 42.2° are marked.

the zeolite spatial confinement effects. In this regard, these particles are likely embedded within the zeolite particles; this attribution will be strengthened by additional characterizations shown below. However, the rather dramatic reaction apparent activation energy drop when Pd loading increases from 3 to 5% (Table 1) suggests that considerable amount of PdO on the 5% Pd sample may stay on the external surface. More discussions will be given below in this regard. The lower panel of Figure 2 displays lower magnification images for the samples with 3% Pd on the various supports. Rather uniformly dispersed PdO particles, measuring 4.9 ± 1.2 nm, are observed on Pd/Al_2O_3 (Figure 2f). For the 3% Pd SSZ-13(6) sample, PdO particles are not resolved at this magnification due to their small sizes (Figure 2g). For 3% Pd SSZ-13 samples with increased Si/Al ratios (Figure 2h–j), external surface PdO particles are readily imaged. For the 3% Pd SSZ-13(12) sample, occasional external surface PdO particles measuring 12.1 ± 3.9 nm are detected. However, as will be shown below, only ~20% of Pd in this catalyst is finely dispersed (Table 1). Therefore, we assume that the majority of PdO particles on this sample are embedded inside zeolite particles but are not readily imaged. Their particle sizes are not readily determined by STEM. Reasonable estimations will be provided below via other characterization techniques. By examining multiple images, the average PdO particle sizes are estimated to be 5.1 ± 2.2 and 5.2 ± 3.3 nm, respectively, for the samples with Si/Al ratios of 24 and 36. For selected samples, PdO particle size distribution histograms are presented in Figure S11 of the Supporting Information. Average particle size values will be used below for PdO surface exposure estimations.

Because of the highly localized nature of STEM imaging and the high electron beam sensitivity of the SSZ-13(6) support that precludes repeated imaging of the same area to improve resolution, we applied XRD next to obtain further information on the nature of Pd in the 3% Pd/SSZ-13 samples.

Figure 3 presents XRD patterns for the 3% Pd/SSZ-13 catalysts. PdO reflection at 34.1° is observed on all catalysts, whereas the one at 42.2° is only apparent on 3% Pd/SSZ-13(36). No metallic Pd reflections are observed, as expected. With increasing Si/Al ratio, the 34.1° features display an approximate intensity ratio of 1:1:2.5:7.5, i.e., PdO particles become larger as support Si/Al ratio increases. The similar PdO reflection intensities for Pd/SSZ-13(6) and Pd/SSZ-13(12) suggest that the majority of PdO particles in these two samples are similar in size, except that the latter sample contains some occasional very large PdO particles (Figure 2h). Therefore, we tentatively suggest that the majority of PdO particles in this catalyst also have an average particle size of 2.5 ± 1.5 nm. It is interesting to note that Pd/SSZ-13(36) displays PdO reflection at 34.1° ~3 times stronger than that of Pd/SSZ-13(24), yet TEM imaging shows comparable PdO particle sizes for these two samples (Figure 2i, j). A likely explanation is that the Pd/SSZ-13(24) sample contains more smaller particles that are less sensitive to XRD; it is well-known that XRD is disproportionally more sensitive to larger particles. The smaller surface area of SSZ-13(36) as compared to other SSZ-13 supports (Table 1) is partially responsible for the larger PdO particles in this sample.

We suggested above that PdO particles in the Pd/SSZ-13(6) catalysts (except the 5% Pd one) are likely encapsulated based on their rather uniform sizes. To confirm this, atom probe tomography (APT), the only material analysis technique that offers both 3D imaging and chemical composition measurements at the atomic scale,[32−34] was used next to probe Pd distribution within the bulk of the 2% Pd/SSZ-13(6) sample (Figure 4). Figure 4a presents 3D distributions of Si, Al, O, and Pd. Si, Al, and O are rather uniformly dispersed as expected. Figures 4b and c depict Pd distribution alone: the majority of Pd atoms are uniformly dispersed within the zeolite bulk (e.g., isolated cations in exchange positions[30,31]); in scattered locations, Pd enrichment is evident (highlighted in Figure 4c). These latter Pd species are assigned to PdO particles embedded in the zeolite particles. Figure 4d plots Si, Al, O, and Pd distributions in the vicinity of selected PdO particles. It is important to note that within ~1 nm around these particles, there is strong Al enrichment and Si depletion. Two possible explanations can be considered: (1) because these PdO particles are a few nanometers in size, too bulky for individual chabazite pore cavities to accommodate,[35] the space needed for such embedded PdO particles must be created at the expense of destruction of a number of neighboring zeolite unit cells. The debris (a mixture of Al_2O_3 and SiO_2 species) thus generated displays a marked distribution around the PdO particles, where Al_2O_3 shows stronger affinity toward PdO, as expected. (2) In SSZ-13 supports, particularly the ones at low Si/Al ratios, the presence of extraframework Al is common.[36] The accumulation of such Al moieties around PdO is also anticipated to occur during catalyst preparation. Even though

https://doi.org/10.1021/jacsau.0c00109
JACS Au 2021, 1, 396−408

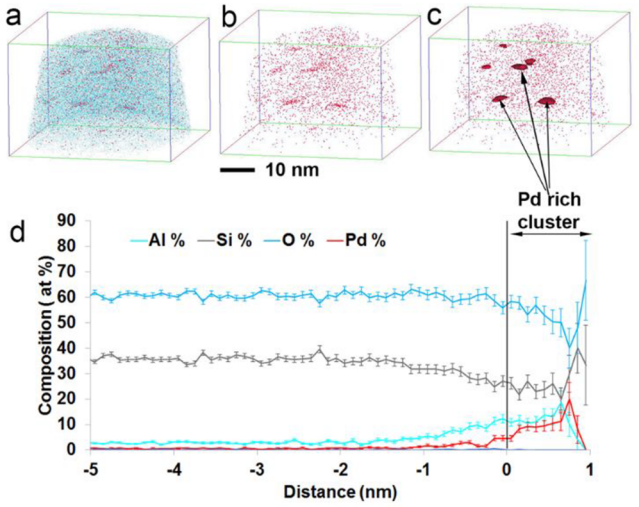

Figure 4. APT results for 2% Pd/SSZ-13(6). (a) 3D Al, Si, O, and Pd distribution. (b) 3D Pd distribution. (c) 3D Pd distribution with Pd enriched regions highlighted. (d) Al, Si, O, and Pd composition in the vicinity of selected Pd-enriched regions. Before imaging, the catalyst was stabilized under wet (2.5% H_2O) methane combustion conditions for ∼20 h at ∼400 °C.

APT analysis allows us to definitively confirm the presence of encapsulated PdO particles in SSZ-13(6), it is important to note that this technique is highly localized and cannot be used for quantifying all PdO in our catalysts.

The methane combustion kinetics and the catalyst characterization results demonstrate a rather clear, even if somewhat qualitative picture, for Pd dispersion in SSZ-13: (1) Pd tends to diffuse into the low Si/Al ratio zeolite particles, but prefers to stay on high Si/Al ratio zeolite external surfaces as PdO. (2) For the Pd moieties that diffuse into zeolite particle, they tend to stay finely dispersed at low loadings; however, encapsulated PdO forms as Pd loading increases. With further increasing Pd loading, external surface PdO also forms on low Si/Al ratio supports. In the next section, some mechanistic insights regarding the complex Pd location and dispersion in SSZ-13 are suggested.

In preparing our Pd/SSZ-13 catalysts, $Pd(NO_3)_2$ solution treated with ammonia was used as the Pd precursor, which was impregnated on NH_4/SSZ-13, and then the solid was calcined in static air at 500 °C. The nature of the Pd precursor during impregnation is likely $Pd(NH_3)_4(NO_3)_2$. It is not clear if this species is too bulky to diffuse into chabazite pores during catalyst preparation. If inward diffusion is permitted, then all Pd sites inside zeolite particles, including finely dispersed Pd sites and PdO, are derived from such Pd-amine complexes. If these complexes cannot diffuse into zeolite pores, then under the high temperature pretreatment conditions, they will first decompose to external surface PdO and then diffuse into zeolite pores via a mechanism suggested by Bell and coauthors,[37] and later confirmed by Okumura et al.:[38,39]

$$(PdO)_n \rightarrow (PdO)_{n-1} + [PdO] \quad \text{(R1)}$$

$$2Z\text{-}H^+ + [PdO] \rightarrow Z^-H^+[PdO]H^+Z^- \quad \text{(R2)}$$

where $(PdO)_n$ denotes external surface PdO particle, [PdO] denotes neutral single Pd intermediate, Z^- denotes zeolite framework charge, and H^+ denotes Brønsted acid proton. According to this mechanism, a pair of Brønsted acid sites at the chabazite pore opening (8-membered ring opening) are critically important for the inward diffusion of the [PdO] units. This is consistent with the experimental finding here that low Si/Al ratio facilitates Pd dispersion. Upon entering the zeolite particle, the [PdO] unit can undergo a number of transformations by interacting with available paired Brønsted acid sites to form isolated monomeric Pd^{2+}, $[Pd(OH)]^+$, or dimeric $[Pd-O-Pd]^{2+}$ sites.[40−42]

$$Z^-H^+[PdO]H^+Z^- \rightarrow Z^-[PdOH]^+H^+Z^- \quad \text{(R3)}$$

$$Z^-H^+[PdOH]^+Z^- \rightarrow Z^-Pd^{2+}Z^- + H_2O \quad \text{(R4)}$$

$$Z^-H^+[PdO]H^+Z^- + [PdO] \rightarrow Z^-[Pd-O-Pd]^{2+}Z^- + H_2O \quad \text{(R5)}$$

To verify if PdO inward diffusion occurs at 500 °C, we prepared a physical mixture of PdO and NH_4/SSZ-13 containing 1 wt % Pd and calcined it at 500 °C in air. Subsequent CO titration monitored with FTIR clearly demonstrated PdO redispersion (Figure S12 of the Supporting Information). However, we cannot rule out the occurrence of inward diffusion of Pd-amine complexes at certain stages of our catalyst synthesis. Regardless, it is important to note that paired Brønsted acid sites at zeolite pore mouths are critical for Pd diffusion into zeolite particles.

We note that the presence of $[Pd(OH)]^+$ and dimeric $[Pd-O-Pd]^{2+}$ sites have not been experimentally confirmed; however, theoretical calculations suggest their presence. When paired Brønsted acids that stabilize such finely dispersed Pd moieties are fully consumed, the remaining in-particle Pd species (originated either from external surface PdO or Pd-amine complexes) will have to agglomerate to form encapsulated PdO particles. As shown above, such particles are rather uniformly dispersed, believed to be caused by zeolite confinement effects, and their surfaces are decorated by a layer of Al-rich oxides. It is anticipated, however, that the inward [PdO] (or Pd-amine) diffusion process cannot proceed indefinitely when Pd loading keeps increasing. For our 5% Pd/SSZ-13(6) catalyst, a considerable amount of PdO is expected to be on the external surface because this catalyst displays rather different kinetic behavior as compared to the 2−3% Pd/SSZ-13(6) samples (Table 1). For SSZ-13 supports with high Si/Al ratios, paired Brønsted acid sites at pore openings are anticipated to decrease sharply. This eliminates inward Pd diffusion, resulting in the predominance of external surface PdO. Such PdO particles display stronger size heterogeneity, and their surfaces are less likely decorated with Al_2O_3.

To establish rigorous structure−activity correlations, ideally all possible Pd species are precisely quantified in all samples studied here. Among which, the quantification of PdO appears to be the most important because the finely dispersed species are much less active than PdO (Figure 1). Even though STEM and APT readily detect PdO particles, both techniques suffer from sampling volume limitations and may not be sensitive enough to small embedded PdO particles. Next, temperature-programmed PdO decomposition (TPD, $PdO \rightarrow Pd + {}^1/_2O_2$) and EXAFS were used to provide further elaboration of the Pd states.

PdO (particles, and possibly clusters that escape from imaging) quantification was done by measuring O_2 desorption from TPD of the Pd/SSZ-13 catalysts; calibration was done by

https://doi.org/10.1021/jacsau.0c00109
JACS Au 2021, 1, 396−408

conducting the same measurement on a 1% Pd/Al_2O_3. The O_2 desorption profiles are shown in Figure 5a, b. For the series of

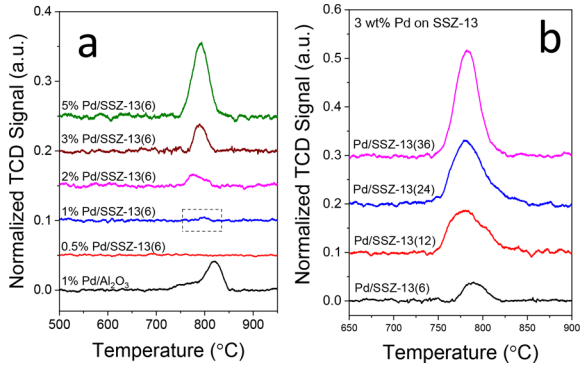

Figure 5. O_2 desorption profiles during temperature-programmed decomposition of PdO phases in Pd/SSZ-13 with (a) different Pd loadings at Si/Al = 6 and (b) different Si/Al ratios at a Pd loading of 3 wt %. A reference 1% Pd/Al_2O_3 TPD profile is included in panel a. Gas feed composition: 10% O_2/He, 50 mL/min. Temperature ramping rate: 10 °C/min.

Pd/SSZ-13(6) samples (Figure 5a), O_2 desorption is undetectable in the 0.2% Pd (not shown) and 0.5% Pd samples. The 1% Pd/SSZ-13(6) sample only generates tiny amount of O_2 (corresponding to $\sim 6.4 \times 10^{-3}$ wt % of PdO, highlighted with a dashed rectangle). For samples that contain more Pd, O_2 yield increases with increasing Pd loading. For the 3% Pd/SSZ-13 samples at other Si/Al ratios (Figure 5b), O_2 yield increases with increasing Si/Al ratio. Note that all O_2 desorption shown in Figure 5 is due entirely to decomposition of Pd-containing moieties. Our control experiments revealed no O_2 formation from the Al_2O_3 and SSZ-13 supports at such temperatures (Figure S13). PdO particles, both inside and outside zeolite particles, obviously will decompose to release O_2 during TPD. Regarding the finely dispersed Pd moieties, note that exchanged Pd^{2+} ions coordinate with zeolite lattice oxygens; such oxygens do not desorb during TPD. However, finely dispersed Pd sites that contain extralattice oxygen, e.g., $[PdOH]^+$ and $[Pd-O-Pd]^{2+}$, should decompose to form O_2. The lack of detectable O_2 desorption from the 0.2% and 0.5% Pd/SSZ-13(6) samples suggests that exchanged Pd^{2+} ions dominate among finely dispersed Pd sites. However, we cannot fully rule out the presence of extremely small quantities of $[PdOH]^+$ and $[Pd-O-Pd]^{2+}$ sites in our catalysts. In any case, the O_2 peaks in Figure 5 are readily attributed to PdO decomposition; the quantified PdO contents in different samples are tabulated in Table 1.

Next, ex situ EXAFS studies were carried out on fresh and spent (~6 h methane oxidation at 400 °C) 0.5–5% Pd/SSZ-13(6) catalysts in their ambient forms. Such measurements serve two purposes: (1) probing Pd dispersion as a function of Pd loading with yet another "bulk" technique and (2) revealing if marked changes occur to the Pd active sites during low-temperature methane combustion. The fresh 0.5–1% Pd/SSZ-13(6) catalysts (Figures 6a and S14) only display first shell Pd–O scattering, consistent with the dominance of isolated Pd^{2+} cations. The X-ray absorption near edge structure spectra (XANES) energies, Table 2, and Figures S15 and S16 are also consistent with Pd^{2+} cations. In copper exchanged SSZ-13, it has also been shown that higher shell peaks are absent in ambient samples.[43,44] The fresh 2–5% Pd/SSZ-13(6) catalysts

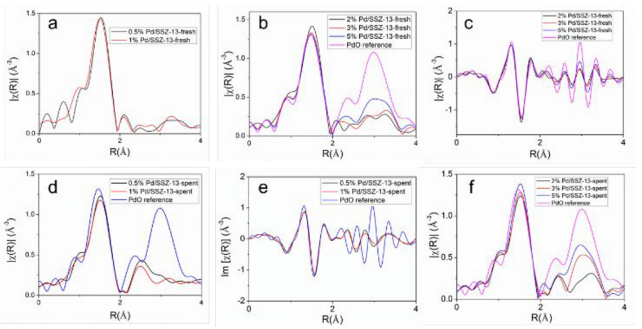

Figure 6. Pd K edge EXAFS spectra for fresh and used Pd/SSZ-13(6) catalysts. (a) Pd K edge EXAFS magnitude spectra for 0.5% Pd/SSZ-13-fresh (black) and 1% Pd/SSZ-13-fresh (red). (b) Pd K edge EXAFS magnitude spectra for 2% Pd/SSZ-13-fresh (black), 3% Pd/SSZ-13-fresh (red), 5% Pd/SSZ-13-fresh (blue), and PdO reference (magenta). (c) Pd K edge EXAFS imaginary spectra for 2% Pd/SSZ-13-fresh (black), 3% Pd/SSZ-13-fresh (red), 5% Pd/SSZ-13-fresh (blue), and PdO reference (magenta). (d) Pd K edge EXAFS magnitude spectra for 0.5% Pd/SSZ-13-spent (black), 1% Pd/SSZ-13-spent (red), and PdO reference (blue). (e) Pd K edge EXAFS imaginary spectra for 0.5% Pd/SSZ-13-spent (black), 1% Pd/SSZ-13-spent (red), and PdO reference (blue). (f) Pd K edge EXAFS magnitude spectra for 2% Pd/SSZ-13-spent (black), 3% Pd/SSZ-13-spent (red), 5% Pd/SSZ-13-spent (blue), and PdO reference (magenta).

Table 2. EXAFS Fitting Parameters for Fresh and Spent Cu/SSZ-13(6) Catalysts

catalyst	edge energy (eV)	scattering pair	coordination number	bond distance (Å)	σ^2 (Å^2)
0.5% Pd, fresh	24 357	Pd–O	3.8	2.01	0.001
1% Pd, fresh	24 357	Pd–O	4.2	2.00	0.001
2% Pd, fresh	24 357	Pd–O	4.2	2.00	0.001
3% Pd, fresh	24 357	Pd–O	4.1	2.00	0.001
5% Pd, fresh	24 357	Pd–O	4.0	2.01	0.001
0.5% Pd, spent	24 357	Pd–O	2.5	2.01	0.001
			1.1	2.06	0.001
1% Pd, spent	24 357	Pd–O	2.9	2.01	0.001
			0.8	2.06	0.001
2% Pd, spent	24 357	Pd–O	3.8	2.01	0.001
3% Pd, spent	24 357	Pd–O	3.9	2.01	0.001
5% Pd, spent	24 357	Pd–O	4.0	2.01	0.001

show significant second shell scattering that match the PdO reference second shell peaks both in the FT-magnitude (Figure 6b) and FT-imaginary (Figure 6c) spectra. Consistent with Figure 5a, the intensity of the second shell increases with increasing Pd loading.

For the spent catalysts, the XANES of the 0.5% and 1% Pd/SSZ-13(6) samples show slight changes in the shape (Figure S16) but no change in the edge energy (Table 2). The EXAFS (Figure 6d) show small second shell oscillations at ~2.4 Å (phase shift uncorrected) that are not present in the fresh catalysts. These signals do not match the PdO reference (Figure 6d, f), and they disappear upon calcination of the spent

https://doi.org/10.1021/jacsau.0c00109
JACS Au 2021, 1, 396–408

catalysts at 500 °C (Figure S14). Previous studies revealed that Pd supported on zeolites can undergo repeated agglomeration−dispersion upon cyclic reduction−oxidation treatments.[45] In this sense, the ∼2.4 Å scatters may be due to exceedingly small PdO clusters that do not display measurable second-shell scattering as bulk PdO that form during methane combustion. Note that such clusters will certainly redisperse during oxidizing treatment at 500 °C. However, considering that our methane combustion reaction conditions are highly oxidizing (not reducing), agglomeration of finely dispersed Pd sites is not considered likely. Furthermore, because PdO is much more active than the finely dispersed Pd sites, one would expect catalyst activity increases with time-on-stream if PdO forms during reaction. However, this was never observed on our Pd/SSZ-13(6) catalysts. Furthermore, the ∼2.4 Å scatters are unlikely due to metallic Pd that forms during methane combustion. In addition to the highly oxidizing reaction conditions that preclude such chemistry, we note that such scatters only appear in spent catalysts with low Pd loadings (i.e., high Pd dispersions). It is highly unlikely that finely dispersed Pd species are more readily reduced than PdO nanoparticles. In studying Pd/HZSM-5, Okumura et al.[39] discovered similar features and suggested that these signals are due to Pd−Al/Si scattering. In dehydrated Cu/SSZ-13 catalysts, similar second shell oscillations have been attributed to Cu−O−Si scattering.[43] On these bases, we suggest that the second shell scatters in the spent 0.5−1% Pd/SSZ-13(6) catalysts are due to formation of Pd−O−Al/Si bonds. To form such bonds, exchanged Pd^{2+} will have to overcome the framework charge attraction to become mobile and then interact with zeolite defects (e.g., terminal Si−OH and Al−OH sites, or extraframework Al, $[Al]_{ex}$−OH). Tentative reaction pathways are suggested as follows:

$$Z^-Pd^{2+}Z^- + H_2O \rightarrow Z^-[PdOH]^+ + H^+Z^- \quad \text{(R6)}$$

$$Z^-[PdOH]^+ + H_2O \rightarrow Pd(OH)_2 + H^+Z^- \quad \text{(R7)}$$

$$Si - OH + Pd(OH)_2 \rightarrow Si - O - Pd(OH) + H_2O \quad \text{(R8)}$$

$$Al - OH + Pd(OH)_2 \rightarrow Al - O - Pd(OH) + H_2O \quad \text{(R9)}$$

$$[Al]_{ex} - OH + Pd(OH)_2 \rightarrow [Al]_{ex} - O - Pd(OH) + H_2O \quad \text{(R10)}$$

In proposing these reaction pathways, it is assumed that (1) charge neutral $Pd(OH)_2$ is more mobile and reactive than charged Pd moieties and (2) thus formed Si/Al−O−Pd bonds have similar bond angle and length, giving rise to indistinguishable scatters at ∼2.4 Å. Spectrum simulation gives Si/Al−O−Pd moiety contents of 0.15 and 0.22 wt %, respectively, in spent 0.5% and 1% Pd/SSZ-13(6) samples. The spent 2−5% catalysts (Figure 6f), on the other hand, still show similar PdO scattering in the second shell as the fresh catalysts. The EXAFS fitting parameters for the fresh and used catalysts are tabulated in Table 2. We also attempted linear combination XANES spectra fits to quantify Pd^{2+} and PdO in our catalysts. Due to the high similarity between Pd/SSZ-13 catalysts and the PdO reference, this was not fruitful (Figure S15).

Structure−Activity Correlations

As reaction kinetics data in Figure 1 suggest, PdO displays much higher activity than finely dispersed Pd moieties for low-temperature methane combustion. For our catalysts that contain large quantities of PdO, i.e., Pd/SSZ-13(6) catalysts with Pd loadings of 2% and above, and 3% Pd on Al_2O_3 and other SSZ-13 supports, it is safely concluded that methane combustion occurs predominately on PdO. Because Pd^{2+}−O^{2-} pairs on PdO surfaces are the active sites under our low-temperature, highly oxidizing conditions,[5] PdO dispersion (D_{PdO}) estimation is imperative for calculating reaction turnover rates, which allows for more rigorous comparisons among the catalysts studied here. Dispersion of supported PdO (D_{PdO}) is commonly done by reducing PdO to Pd and then measuring the surface sites with H_2, CO, or H_2−O_2 titration.[46] We attempted H_2−O_2 titration but could not obtain reliable results: for the 2−5% Pd/SSZ-13(6) catalysts, prereduction with H_2 also converts the finely dispersed Pd cations to Pd nanoparticles, thus giving rise to erroneous results; for 3% Pd supported on other SSZ-13 supports with higher Si/Al ratios, extensive Pd sintering occurs during prereduction as a result of weak Pd−support interactions. Therefore, D_{PdO} was calculated in the following using the estimated PdO particle sizes via STEM assuming spherical particle shape, surface "Pd^{2+}−O^{2-}" density of 1.41×10^{-5} mol/m^2, and PdO bulk density of 6.78×10^4 mol/m^3.[47] Based on average particle sizes derived from STEM images (a few examples are shown in Figure S11) and particle size-PdO dispersion correlation described in Figure S17, D_{PdO} values were readily obtained (Table S1).

Based on the PdO contents and D_{PdO} values, CH_4 conversion rates over PdO-dominant catalysts in Figure 1 were converted to turnover rates (TORs) on a per surface Pd^{2+}−O^{2-} pair basis, and the results are presented in Figure 7 in the form of Arrhenius plots. 3% Pd/Al_2O_3 displays higher

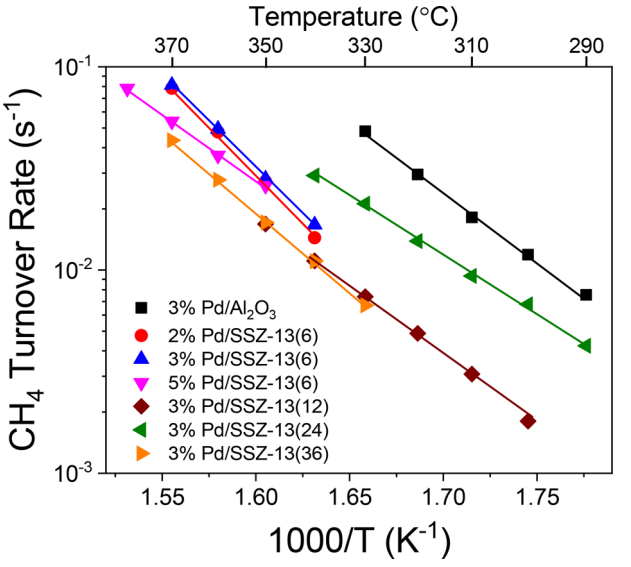

Figure 7. CH_4 combustion turnover rates in the form of Arrhenius plots over PdO-containing Pd/Al_2O_3 and Pd/SSZ-13 catalysts. Gas feed composition: 640 ppm of CH_4, 14% O_2, 5% CO_2, 2.5% H_2O, and balanced N_2. The catalysts were diluted 10 times, and ∼100 mg diluted catalysts were used for each measurement. The total flow was 300 mL/min. Turnover rates were calculated based on PdO content and PdO dispersion in catalysts that contain it, i.e. contribution to CH_4 turnover from the portion of Pd not staying as PdO is neglected.

https://doi.org/10.1021/jacsau.0c00109
JACS Au 2021, 1, 396−408

TORs than any Pd/SSZ-13 catalysts, but the differences are never larger than an order of magnitude. The Pd/SSZ-13 samples show similar TORs. For example, TORs differ by no more than 3-fold at 350 °C over these Pd/SSZ-13 catalysts. This leads to an important conclusion that PdO particles supported on SSZ-13 display at best very weak structure sensitivity in methane combustion, irrespective of their location (embedded or not). This is yet another example for structure insensitivity for methane combustion over PdO.[48] However, the 2% and 3% Pd/SSZ-13(6) catalysts show apparent activation energies ∼50 kJ/mol higher than other catalysts (Table 1). Particularly, the 5% Pd/SSZ-13(6) catalyst also displays apparent activation energies close to the 3% Pd/SSZ-13 catalysts with higher Si/Al ratios. Even though we are unable to quantitatively distinguish embedded versus external surface PdO contents in these Pd/SSZ-13(6) catalysts, the substantially higher apparent activation energies for the 2% and 3% Pd/SSZ-13(6) catalysts strongly suggest that (1) the PdO particles in these two samples are mostly (if not all) encapsulated and (2) the zeolite support exerts certain confinement effects that make CH_4 molecules more difficult to activate on such encapsulated particles. CH_4 combustion on external surface PdO, on the other hand, does not experience such a confinement effect; as such, lower apparent activation energies are registered. Next, discussions are given to samples in which PdO does not dominate.

Via STEM (Figure 2) and EXAFS (Figure 6) measurements, PdO is not detected in our 1% Pd/SSZ-13(6) sample. However, O_2 TPD (Figure 5a) confirms the presence of small amount of PdO (∼6.4×10^{-3} wt%) in this catalyst. On the basis that PdO is more active than finely dispersed Pd sites, it is possible that the majority of CH_4 turnovers are sustained by the minority PdO in this catalyst. This notion is verified by TOR estimations shown as follows. The average size of the PdO particles within this sample is unknown; however, it is reasonable to assume that it is the same as PdO particles in the 2% Pd/SSZ-13(6) sample (i.e., 2.5 ± 1.5 nm, D_{PdO} = 0.25). Based on this, a TOR of ∼2.0 s^{-1} at 450 °C is readily obtained, assuming that methane oxidation is entirely catalyzed by PdO. Using the Arrhenius plots for the 2% and 3% Pd/SSZ-13(6) samples shown in Figure 7, a simple extrapolation to 450 °C reveals a TOR of ∼3.0 s^{-1}. The similarity between these two TORs strongly suggests that the active sites in the 1% Pd/SSZ-13(6) catalyst are indeed the minority PdO sites. This notion is further corroborated by the fact that this sample displays rather similar apparent activation energies and reactant orders as the 2% Pd/SSZ-13(6) catalyst (Table 1). Following the same analogy, we further suggest that the active sites in the 0.5% Pd/SSZ-13(6) sample are also minority PdO sites, even though in this catalyst, the amount of PdO is too small to be verified by O_2 TPD. Note particularly that the 0.5% Pd/SSZ-13(6) and the 1% Pd/SSZ-13(6) sample also display strikingly similar kinetic behavior (Figure 1b and Table 1). We note that this finding here is a good point of warning for single atom catalysis studies that emerged as an active new frontier in heterogeneous catalysis in recent years:[49−51] for catalytic systems where rate-limiting steps (e.g., C−H activation here) are orders of magnitude more facile on multinuclear active sites, the majority of catalytic turnovers can be sustained by such minority sites even when their content is too low for most characterization methods to reliably determine.

Finally, it is suggested that PdO is absent in the 0.2% Pd/SSZ-13(6) catalyst, and methane combustion is primarily carried out on the finely dispersed Pd sites. This notion is supported by the facts that (1) this catalyst is orders of magnitude less active than any other catalysts studied here, and (2) this catalyst displays distinct CH_4 and O_2 pressure orders. From the discussions above, this catalyst contains exchanged Pd^{2+} and a few possible monomeric and dimeric Pd sites that contain extra lattice oxygen (R3, R5) in the fresh form. Although the spent form of this catalyst was not examined via EXAFS, based on measurements done on the spent 0.5% and 1% Pd/SSZ-13(6) samples (Figure 6d), it is reasonable to assume that some of such sites can relocate to form Pd−O−Al/Si moieties during methane combustion (R8−R10). Under our low-temperature, highly oxidizing, and steady-state reaction conditions, studies by Chin et al. demonstrated that Pd cation-lattice oxygen pairs (Pd^{2+}−O^{2-}) are the active sites for heterolytic C−H activation, the rate-limiting step for methane combustion.[5,52] Adopting this theory, we postulate that in the 0.2% Pd/SSZ-13(6) catalyst, active sites are also in the form of Pd−O pairs. It is also reasonable to assume that Pd paired with extra lattice oxygen is more active than Pd paired with lattice oxygen. Regardless of the exact nature of the active sites, the markedly lower CH_4 order over this catalyst than any other samples studied here implies reversible C−H activation, i.e., $CH_4 + Pd^{2+} - O^{2-} \rightleftharpoons H_3C^{\delta-}\cdots Pd_{ox}\cdots H^{\delta+}\cdots O_{ox}^{\ddagger}$.[5] This is consistent with the exceptionally high O_2 pressure order for this catalyst, i.e., weak O_2 chemisorption and activation for this catalyst rendering CH_3 intermediates not immediately consumed upon formation, e.g., to CH_2OH intermediates by reacting with an active oxygen.[53] It is interesting to note that the weak methane activation behavior for finely dispersed Pd species, albeit not ideal for methane total combustion, may find use for partial oxidation of methane. This, however, is not explored here. Note that in studying Pd/H-ZSM-5, Resasco and coworkers also discovered the much lower activity of Pd cations than PdO in catalyzing methane combustion.[40] In a more recent study by Goodman et al.,[54] the authors also demonstrated PdO dispersing into single atoms as a cause for catalyst deactivation in methane combustion.

Structure−Stability Correlations

Reaction results shown in Figures S7−S10 demonstrate that 3% Pd/SSZ-13(6, 12) catalysts display similar H_2O-induced deactivation rates as 3% Pd/Al_2O_3, much faster than the 3% Pd/SSZ-13(24, 36) catalysts. Pd/Al_2O_3 deactivation in the presence of water vapor has been extensively described in literature.[3] The fact that unsupported PdO does not suffer from this type of deactivation[55] leads naturally to a hypothesis that the Al_2O_3 support and/or the PdO-Al_2O_3 interface play important roles in catalyst deactivation. Assuming that the support and/or interface contribute to O_2 activation to replenish surface oxygen consumed in methane combustion, then Al_2O_3 hydroxylation, which slows O_2 activation, appears to be a good explanation to H_2O-induced deactivation.[16] This support hydroxylation mechanism also explains deactivation of the highly active Pd core−CeO_2 shell methane combustion catalyst.[1,56] However, none of our SSZ-13 supports is anticipated to readily hydroxylate under our methane combustion conditions. The APT results shown in Figure 4 provide important structural information that the embedded particles are decorated by a layer of Al_2O_3, likely originated from (1) destruction of zeolite unit cells for these particles and (2) migration of extraframework Al toward embedded PdO. Even for the PdO particles that are located on the zeolite

https://doi.org/10.1021/jacsau.0c00109
JACS Au 2021, 1, 396−408

external surface, PdO-Al_2O_3 affiliation is considered a strong driving force for extraframework Al to migrate and decorate the PdO particles. However, because the amount of extraframework Al decreases sharply with increasing Si/Al ratio,[36] the external surface PdO particles on SSZ-13(24, 36) supports are much less vulnerable to Al decoration. Overall, the embedded PdO particles undergo similar PdO-Al_2O_3 interactions as those in Pd/Al_2O_3 (or even stronger due to entire encapsulation), whereas such interactions are weak or absent on 3% Pd/SSZ-13(24, 36). Such a difference is believed to the main reason why our 3% Pd/SSZ-13(6, 12) catalysts deactivate at comparable rates as Pd/Al_2O_3, whereas our 3% Pd/SSZ-13(24, 36) catalysts deactivate much slower. It is important to note that PdO encapsulation itself is not responsible for catalyst deactivation. Recent study by Wang et al. demonstrated that PdO confined in pure silica zeolite silicalite-1 displays considerable stability during low-temperature methane combustion in the presence of H_2O.[57] We note that their findings are fully consistent with what we observe in the present study: the use of pure silica support precludes any PdO-Al interactions that cause rapid catalyst deactivation. It is interesting to note from Table 1 that the H_2O pressure order also differs considerably for Pd/SSZ-13 catalysts with different Si/Al ratios. Particularly, the close-to-zero H_2O orders for 3% Pd/SSZ-13(24, 36) should also be considered beneficial to catalyst stability. However, because unsupported PdO also displays a −1 H_2O order during low-temperature methane combustion[48] but obviously does not suffer from this type of deactivation,[55] PdO-Al interactions should be considered primarily responsible for H_2O-induced catalyst deactivation.

General Discussions on Fundamentals and Applications

Under low-temperature, highly oxidizing, and steady-state conditions where Pd^{2+}−O^{2-} pairs are the active sites, finely dispersing Pd to the single atom level causes severe activity loss that completely overwhelms benefits gained by the Pd dispersion increase. Our kinetic data show that in 0.2% Pd/SSZ-13(6), Pd^{2+}−O^{2-} pairs are passivated so greatly that the methane pressure order deviates substantially from ∼1, suggesting a rare case of reversibility for the formation of $CH_{3(a)}$ intermediates. Therefore, for designing single atom Pd catalysts for methane combustion, a support material that stabilizes Pd^{2+} and provides highly active O^{2-} must be used to convert $CH_{3(a)}$ intermediates immediately upon their formation. For "traditional" catalysts with PdO nanoparticle active sites, we show here that by avoiding PdO-Al_2O_3 interactions, H_2O-induced catalyst deactivation slows. Therefore, in designing practical catalysts from low-temperature methane combustion, avoiding the use of supports that undergo facile hydroxylation should be considered. Finally, for methane combustion by PdO under O_2-rich conditions, C−H bond cleavage on Pd^{2+}−O^{2-} pairs has been identified as the rate-limiting step under kinetic control.[5,28] In this case, turnover rates are not strongly perturbed by the support of choice, support confinement effects, and even the introduction of transition metal additives (generally described as weak structure sensitivity).[11,12] However, for emission control catalysis, (nonsteady state) operations out of kinetic control is frequent.[8−10,58] In this case, rapid O_2 activation and oxygen delivery from the support to PdO can become rate-limiting for methane conversion. In addition to strong PdO anchoring, rapid oxygen delivery (e.g., the core−shell catalyst synthesis concept[1,56]) is another key for successful catalyst design for low-temperature applications.

CONCLUSION

By tuning SSZ-13 support Si/Al ratios and by varying Pd loadings, well-defined Pd/SSZ-13 catalysts containing three different methane combustion active sites, i.e., finely dispersed Pd cations, PdO nanoparticles embedded in zeolite, and PdO nanoparticles deposited on zeolite external surface, are prepared. Kinetics studies show that finely dispersed Pd sites are much less active than PdO nanoparticles due mainly to their reluctance in activating C−H and O_2. Embedded and external surface PdO nanoparticles show similar activity under our test conditions. The embedded particles display apparent reaction activation energies ∼50 kJ/mol higher than external surface PdO, likely due to confinement constraints to methane activation. Pd/SSZ-13 catalysts display markedly different deactivation rates in the presence of water vapor, where catalysts with higher Si/Al ratios exhibit much slower deactivation rates. Via atom probe tomography studies, it is revealed that the embedded PdO nanoparticles are decorated with an Al_2O_3-rich layer, thus suffering from the same deactivation mechanism as industrial Pd/Al_2O_3 catalysts. In contrast, the external surface PdO nanoparticles supported on high Si/Al ratio supports do not suffer from this deactivation mechanism.

EXPERIMENTAL SECTION

Synthesis of SSZ-13 Supports and Catalysts

Na/SSZ-13 zeolites with different Si/Al ratios were prepared with a hydrothermal method. For a typical synthesis of Na/SSZ-13 with a Si/Al ratio of 6 (gel molar composition 10.8 SDA:2.7 NaOH:1 Al_2O_3:13.5 SiO_2:498 H_2O), 0.8 g NaOH (Sigma-Aldrich, ≥99%) was dissolved in 52 mL of deionized water. TMAda−OH (17.1 g, Sachem Inc., 25% *N,N,N*-trimethyl-1-adamantyl ammonium hydroxide) was added as the structure directing agent (SDA). $Al(OH)_3$ (1.5 g, Sigma-Aldrich, ∼54% Al_2O_3) was added to the solution and stirred at 400 rpm until it was completely dissolved. LUDOX HS-30 colloidal silica (20.0 g, Sigma-Aldrich, 30 wt % suspension in H_2O) was added slowly to the solution until a uniform white gel was formed. The gel was sealed in a 125 mL Teflon-lined stainless-steel autoclave; the latter was then placed in a sand-bath on top of a hot plate stirrer. A magnetic stir bar was placed inside the autoclave, allowing continuous gel agitation. The synthesis was carried out at 160 °C for 96 h under continuous stirring at 400 rpm. The final product was separated by centrifugation and washed three times with deionized water. The solid was dried overnight at 60 °C, followed by calcination at 650 °C in static air for 5 h to burn off the SDA. To prepare SSZ-13 with other Si/Al ratios, quantities for $Al(OH)_3$ and HS-30 were adjusted accordingly. For Si/Al = 12, the mixture gel contained 1.51 g of $Al(OH)_3$, 40.0 g of HS-30, and 38.4 g of deionized water. For Si/Al = 24, the $Al(OH)_3$ amount was decreased to 0.75 g, while other components maintained the same as for Si/Al = 12 synthesis. For Si/Al = 36, the $Al(OH)_3$ amount was further reduced to 0.5 g with the other components maintained the same as for Si/Al = 12 synthesis.

The Na/SSZ-13 zeolites thus synthesized were converted to NH_4/SSZ-13 by ion exchange with 0.1 M NH_4NO_3 solution. Na/SSZ-13 (1.0 g) was dispersed in 100 mL of 0.1 M NH_4NO_3 solution, and exchange was carried out at 80 °C for 2 h under stirring. The solid was recovered by centrifugation and washed with deionized water. To ensure complete Na^+ removal, the exchange process was repeated once. The solid was dried at 60 °C in a N_2 gas flow.

Pd was loaded onto NH_4/SSZ-13 by incipient wetness impregnation. For a typical synthesis, ∼250 mg of $Pd(NO_3)_2{\cdot}2H_2O$ (∼40% Pd basis, Sigma-Aldrich) was dissolved in 8 mL of deionized water; the dissolution was facilitated with sonication. Next, 2 mL of ammonia

https://doi.org/10.1021/jacsau.0c00109
JACS Au 2021, 1, 396−408

solution (Fisher Scientific, 29.6%) was added to coordinate the Pd ions with NH_3 ligands and to adjust the solution pH to ~10. The obtained solution was added to the support drop by drop until incipient wetness. The solids were dried at 60 °C in N_2 gas flow overnight and then calcined at 500 °C in air for 3 h to decompose the nitrate precursor. The Pd/SSZ-13 catalysts thus prepared were used for methane combustion without further treatments. The catalysts are denoted as *x*% Pd/SSZ-13(*y*) in the following, where "*x*" represents Pd content (wt%) and "*y*" represents Si/Al ratio of the support. For comparison, a 3% Pd/Al_2O_3 was prepared with the same incipient impregnation method. The Al_2O_3 used was CATALOX SBa-200 Alumina (mainly γ-Al_2O_3).

Pd Loading Determination

Pd loadings were determined by inductively coupled plasma-optical emission spectroscopy (ICP-OES), measured at Galbraith Laboratories (Knoxville, TN, United States).

Catalyst Surface Area and Porosity

BET surface areas and t-plot micropore volumes of the catalysts were measured with a Quantachrome Autosorb-6 analyzer with liquid N_2 adsorption. The catalysts were degassed under vacuum at a temperature of 150 °C overnight before the tests.

PdO Temperature-Programmed Decomposition (TPD)

In these experiments, ~100 mg of catalyst was used for each measurement. The catalyst was pretreated with 50 mL/min of 10% O_2/He at 200 °C for 2 h to make sure all Pd species are fully oxidized. The sample temperature was then ramped up from 200 to 1000 °C in the same gas flow at a ramping rate of 10 °C/min. O_2 emission was quantified using PdO decomposition of a 1% Pd/Al_2O_3 reference material following the same procedure. The measurements were conducted on a Micromeritics AutoChem II 2920 chemisorption system.

Methane Combustion Rate Measurements

Methane combustion experiments were carried out in a quartz tube plug flow reactor setup. The gas feed was composed of 640 ppm of CH_4, 14% O_2, 5% CO_2, 2.5% H_2O, and balance N_2. The total flow was 300 mL/min. The inlet and outlet gas concentrations were monitored with an online MKS MultiGas 2030 FTIR gas analyzer with the gas cell maintained at 191 °C. Approximately 60 mg of catalyst (without dilution) was used for light-off measurements, and tests at fixed temperatures were conducted for long periods to monitor deactivation. The catalyst was first exposed to the reactants at 400 °C for 6 h for stabilization. Light-off test was conducted afterword, where the catalyst temperature was ramped up from 300 to 600 °C at a rate of 3 °C/min. Then, quasi-steady state measurements were conducted at stepwise decreasing temperatures from 500 to 300 °C with 50 °C intervals. At each temperature, the measurement was continued for ~1 h to obtain an average conversion. These quasi-steady state measurements were repeated one more time to check catalyst stability. Finally, a longer-term stability test was carried out at 400 °C for 50 h on selected catalysts.

Additional reaction measurements were conducted under kinetic controlled regions. In this case, the catalysts were diluted 1−200 times with inert SiO_2 (Sigma-Aldrich silica gel, Davisil, grade 645, precalcined at 600 °C for 5 h to remove possible impurities) to avoid heat and mass transfer limitations. Approximately 120 mg of diluted catalyst was used for such measurements. The reaction mixture is 640 ppm of CH_4, 14% O_2, 5% CO_2, 2.5% H_2O, and balanced N_2. The total flow was 300 mL/min. Methane conversions were maintained below ~10%. Note that the cofed CO_2 and H_2O concentrations were much higher than those from methane combustion, differential conditions were readily maintained in terms of both reactant conversion and product formation. Kinetic data used to calculate apparent activation energies were measured within 300−400 °C at 10 °C intervals. Only data collected at low methane conversions that fell into linear Arrhenius regimes were used for kinetic analysis.

The power-law dependence with respect to the reactants (CH_4, O_2) and the products (CO_2, H_2O) were measured according to the rate expression $r = k{p_{CH_4}}^{\alpha}{p_{O_2}}^{\beta}{p_{H_2O}}^{\gamma}{p_{CO_2}}^{\delta}$. For these measurements, the partial pressures of the individual gases were varied within the following ranges: CH_4 200−1000 ppm, O_2 10−25%, CO_2 1.0−10%, and H_2O 2.5−7.0%. The total flow was maintained at 300 mL/min by adjusting the balance N_2 flow. These reactions were carried out at temperatures that allow ready maintenance of differential conversions.

HAADF-STEM Measurements

High angle annular dark field scanning transmission electron microscopy (HAADF-STEM) measurements were performed with a FEI Titan 80−300 microscope operated at 300 kV. The images were acquired with a HAADF detector with inner collection angle set to 52 mrad. The probe convergence angle was 18 mrad. Note that the SSZ-13 supports, in particular the low Si/Al ratio ones, are very sensitive to electron beam damage. Therefore, all images were acquired with lowest possible electron beam intensities.

APT Measurements

Needle specimens of fresh and used 0.5 and 2% Pd/SSZ-13(6) catalysts were prepared by a direct particle lift-out and annular milling process using a FEI Helios Nanolab 600 Dual beam FIB-SEM system. The APT analysis was conducted using CAMECA LEAP4000XHR atom probe tomography system equipped with a pulsed UV laser (355 nm wavelength). The pulse laser energy was kept at 100pJ; evaporation rate was maintained at 0.005 atoms/pulse, while laser pulse frequency was kept at 125 kHz. Specimen temperature was maintained at 40 K. The APT data were reconstructed and analyzed using the IVAS software.

EXAFS Measurements

In situ XAS experiments were performed at the 10-BM-B beamline at the Advanced Photon Source (APS), Argonne National Laboratory at the Pd K (24.350 keV) edge in transmission mode with energy resolution of 0.6 eV and edge energy precision greater than 0.1 eV. Catalysts were ground into a powder, pressed into a sample holder, and sealed in a sample cell with leak-tight Kapton end-caps.

Each measurement was accompanied by simultaneous measurement of a Pd foil scan obtained through a third ion chamber for internal energy calibration. XAS data was fitted by using Demeter 0.9.25 software package. The edge energy was determined using the maximum of the first peak in the first derivative of the XANES spectra. Least-squares fit in R-space of the k^2-weighted Fourier transform data from 2.7 to 12.0 $Å^{-1}$ was used to obtain the EXAFS coordination parameters. The first shell was used to fit the EXAFS spectra. The amplitude reduction factor (S_0^2) was determined as 0.80 by fitting a reference spectrum of the Pd foil, and then it was used for fitting of all the other EXAFS spectra. Only the first shell of the catalysts was fitted. For 0.5% Pd/SSZ-13(6) and 1% Pd/SSZ-13(6) spent catalysts, two Pd−O paths were included, and eight free parameters were used for the initial fitting. For all other catalysts, one Pd−O path was included, and four free parameters were used for the initial fitting.

■ ASSOCIATED CONTENT

Supporting Information

The Supporting Information is available free of charge at https://pubs.acs.org/doi/10.1021/jacsau.0c00109.

CH_4, O_2, H_2O, and CO_2 power-law dependence plots over Pd/SSZ-13(6) and 3% Pd catalysts; catalyst stability test results (CH_4 conversion versus time-on-stream plots) and the corresponding catalyst deactivation rate constants; O_2 desorption profiles during temperature programmed decomposition of PdO within the catalysts; Pd K edge EXAFS of 0.5% Pd/SSZ-13(6) showing the ~2.4 Å scattering; Pd K edge XANES spectra of 0.5%, 5% Pd/SSZ-13, and PdO reference;

https://doi.org/10.1021/jacsau.0c00109
JACS Au 2021, 1, 396−408

CH_4 combustion turnover rates in the form of Arrhenius plots over PdO-containing Pd/Al_2O_3 and Pd/SSZ-13 catalysts (PDF)

AUTHOR INFORMATION

Corresponding Authors

Feng Gao − *Institute for Integrated Catalysis, Pacific Northwest National Laboratory, Richland, Washington 99354, United States;* orcid.org/0000-0002-8450-3419; Email: feng.gao@pnnl.gov

Yong Wang − *Institute for Integrated Catalysis, Pacific Northwest National Laboratory, Richland, Washington 99354, United States; Voiland School of Chemical Engineering and Bioengineering, Washington State University, Pullman, Washington 99164, United States;* orcid.org/0000-0002-8460-7410; Email: yong.wang@pnnl.gov

Authors

Yanran Cui − *Institute for Integrated Catalysis, Pacific Northwest National Laboratory, Richland, Washington 99354, United States*

Johnny Zhu Chen − *Davidson School of Chemical Engineering, Purdue University, West Lafayette, Indiana 47907, United States;* orcid.org/0000-0003-0697-4351

Bo Peng − *Institute for Integrated Catalysis, Pacific Northwest National Laboratory, Richland, Washington 99354, United States*

Libor Kovarik − *Institute for Integrated Catalysis, Pacific Northwest National Laboratory, Richland, Washington 99354, United States;* orcid.org/0000-0002-2418-6925

Arun Devaraj − *Institute for Integrated Catalysis, Pacific Northwest National Laboratory, Richland, Washington 99354, United States*

Zhe Li − *Department of Chemical and Biological Engineering, Iowa State University, Ames, Iowa 50011, United States*

Tao Ma − *Department of Energy, Ames Laboratory, Ames, Iowa 50011, United States;* orcid.org/0000-0002-0579-8045

Yilin Wang − *Institute for Integrated Catalysis, Pacific Northwest National Laboratory, Richland, Washington 99354, United States*

Janos Szanyi − *Institute for Integrated Catalysis, Pacific Northwest National Laboratory, Richland, Washington 99354, United States;* orcid.org/0000-0002-8442-5465

Jeffrey T. Miller − *Davidson School of Chemical Engineering, Purdue University, West Lafayette, Indiana 47907, United States;* orcid.org/0000-0002-6269-0620

Complete contact information is available at: https://pubs.acs.org/10.1021/jacsau.0c00109

Notes

The authors declare no competing financial interest.

ACKNOWLEDGMENTS

The authors gratefully acknowledge the US Department of Energy (DOE), Energy Efficiency and Renewable Energy, Vehicle Technologies Office for the support of this work. Part of the research described in this paper was performed in the Environmental Molecular Sciences Laboratory (EMSL), a national scientific user facility sponsored by the DOE's Office of Biological and Environmental Research and located at PNNL. PNNL is operated for the US DOE by Battelle. F.G. is grateful to Professors Enrique Iglesia (UC Berkeley) and Cathy Chin (Univ. of Toronto) for fruitful discussions.

REFERENCES

(1) Cargnello, M.; Jaen, J. J. D.; Garrido, J. C. H.; Bakhmutsky, K.; Montini, T.; Gamez, J. J. C.; Gorte, R. J.; Fornasiero, P. Exceptional Activity for Methane Combustion over Modular Pd@CeO2 Subunits on Functionalized Al2O3. *Science* **2012**, *337* (6095), 713−717.

(2) Farrauto, R. J. Low-Temperature Oxidation of Methane. *Science* **2012**, *337* (6095), 659−660.

(3) Ciuparu, D.; Lyubovsky, M. R.; Altman, E.; Pfefferle, L. D.; Datye, A. Catalytic combustion of methane over palladium-based catalysts. *Catal. Rev.: Sci. Eng.* **2002**, *44* (4), 593−649.

(4) Chen, J. H.; Arandiyan, H.; Gao, X.; Li, J. H. Recent Advances in Catalysts for Methane Combustion. *Catal. Surv. Asia* **2015**, *19* (3), 140−171.

(5) Chin, Y. H.; Buda, C.; Neurock, M.; Iglesia, E. Consequences of Metal-Oxide Interconversion for C-H Bond Activation during CH4 Reactions on Pd Catalysts. *J. Am. Chem. Soc.* **2013**, *135* (41), 15425−15442.

(6) Farrauto, R. J.; Hobson, M. C.; Kennelly, T.; Waterman, E. M. Catalytic Chemistry of Supported Palladium for Combustion of Methane. *Appl. Catal., A* **1992**, *81* (2), 227−237.

(7) McCarty, J. G. Kinetics of PdO combustion catalysis. *Catal. Today* **1995**, *26* (3−4), 283−293.

(8) Lyubovsky, M.; Pfefferle, L. Methane combustion over the alpha-alumina supported Pd catalyst: Activity of the mixed Pd/PdO state. *Appl. Catal., A* **1998**, *173* (1), 107−119.

(9) Xiong, H. F.; Wiebenga, M. H.; Carrillo, C.; Gaudet, J. R.; Pham, H. N.; Kunwar, D.; Oh, S. H.; Qi, G. S.; Kim, C. H.; Datye, A. K. Design considerations for low-temperature hydrocarbon oxidation reactions on Pd based catalysts. *Appl. Catal., B* **2018**, *236*, 436−444.

(10) Ferri, D.; Elsener, M.; Krocher, O. Methane oxidation over a honeycomb Pd-only three-way catalyst under static and periodic operation. *Appl. Catal., B* **2018**, *220*, 67−77.

(11) Willis, J. J.; Gallo, A.; Sokaras, D.; Aljama, H.; Nowak, S. H.; Goodman, E. D.; Wu, L. H.; Tassone, C. J.; Jaramillo, T. F.; Abild-Pedersen, F.; Cargnello, M. Systematic Structure Property Relationship Studies in Palladium Catalyzed Methane Complete Combustion. *ACS Catal.* **2017**, *7* (11), 7810−7821.

(12) Willis, J. J.; Goodman, E. D.; Wu, L. H.; Riscoe, A. R.; Martins, P.; Tassone, C. J.; Cargnello, M. Systematic Identification of Promoters for Methane Oxidation Catalysts Using Size- and Composition-Controlled Pd-Based Bimetallic Nanocrystals. *J. Am. Chem. Soc.* **2017**, *139* (34), 11989−11997.

(13) Sekizawa, K.; Widjaja, H.; Maeda, S.; Ozawa, Y.; Eguchi, K. Low temperature oxidation of methane over Pd catalyst supported on metal oxides. *Catal. Today* **2000**, *59* (1−2), 69−74.

(14) Burch, R.; Urbano, F. J.; Loader, P. K. Methane Combustion over Palladium Catalysts - the Effect of Carbon-Dioxide and Water on Activity. *Appl. Catal., A* **1995**, *123* (1), 173−184.

(15) Schwartz, W. R.; Pfefferle, L. D. Combustion of Methane over Palladium-Based Catalysts: Support Interactions. *J. Phys. Chem. C* **2012**, *116* (15), 8571−8578.

(16) Schwartz, W. R.; Ciuparu, D.; Pfefferle, L. D. Combustion of Methane over Palladium-Based Catalysts: Catalytic Deactivation and Role of the Support. *J. Phys. Chem. C* **2012**, *116* (15), 8587−8593.

(17) Persson, K.; Ersson, A.; Jansson, K.; Iverlund, N.; Jaras, S. Influence of co-metals on bimetallic palladium catalysts for methane combustion. *J. Catal.* **2005**, *231* (1), 139−150.

(18) Goodman, E. D.; Dai, S.; Yang, A. C.; Wrasman, C. J.; Gallo, A.; Bare, S. R.; Hoffman, A. S.; Jaramillo, T. F.; Graham, G. W.; Pan, X. Q.; Cargnello, M. Uniform Pt/Pd Bimetallic Nanocrystals Demonstrate Platinum Effect on Palladium Methane Combustion Activity and Stability. *ACS Catal.* **2017**, *7* (7), 4372−4380.

(19) Persson, K.; Pfefferle, L. D.; Schwartz, W.; Ersson, A.; Jaras, S. G. Stability of palladium-based catalysts during catalytic combustion of methane: The influence of water. *Appl. Catal., B* **2007**, *74* (3−4), 242−250.

(20) Gholami, R.; Alyani, M.; Smith, K. J. Deactivation of Pd Catalysts by Water during Low Temperature Methane Oxidation Relevant to Natural Gas Vehicle Converters. *Catalysts* **2015**, *5* (2), 561−594.
(21) Persson, K.; Ersson, A.; Jansson, K.; Fierro, J. L. G.; Jaras, S. G. Influence of molar ratio on Pd-Pt catalysts for methane combustion. *J. Catal.* **2006**, *243* (1), 14−24.
(22) Danielis, M.; Colussi, S.; de Leitenburg, C.; Soler, L.; Llorca, J.; Trovarelli, A. Outstanding Methane Oxidation Performance of Palladium-Embedded Ceria Catalysts Prepared by a One-Step Dry Ball-Milling Method. *Angew. Chem., Int. Ed.* **2018**, *57* (32), 10212−10216.
(23) Colussi, S.; Gayen, A.; Camellone, M. F.; Boaro, M.; Llorca, J.; Fabris, S.; Trovarelli, A. Nanofaceted Pd-O Sites in Pd-Ce Surface Superstructures: Enhanced Activity in Catalytic Combustion of Methane. *Angew. Chem., Int. Ed.* **2009**, *48* (45), 8481−8484.
(24) Zou, X. L.; Rui, Z. B.; Ji, H. B. Core-Shell NiO@PdO Nanoparticles Supported on Alumina as an Advanced Catalyst for Methane Oxidation. *ACS Catal.* **2017**, *7* (3), 1615−1625.
(25) Lim, J. B.; Jo, D.; Hong, S. B. Palladium-exchanged small-pore zeolites with different cage systems as methane combustion catalysts. *Appl. Catal., B* **2017**, *219*, 155−162.
(26) Friberg, I.; Sadokhina, N.; Olsson, L. The effect of Si/Al ratio of zeolite supported Pd for complete CH4 oxidation in the presence of water vapor and SO2. *Appl. Catal., B* **2019**, *250*, 117−131.
(27) Ribeiro, F. H.; Chow, M.; Dallabetta, R. A. Kinetics of the Complete Oxidation of Methane over Supported Palladium Catalysts. *J. Catal.* **1994**, *146* (2), 537−544.
(28) Fujimoto, K.; Ribeiro, F. H.; Avalos-Borja, M.; Iglesia, E. Structure and reactivity of PdOx/ZrO2, catalysts for methane oxidation at low temperatures. *J. Catal.* **1998**, *179* (2), 431−442.
(29) Monteiro, R. S.; Zemlyanov, D.; Storey, J. M.; Ribeiro, F. H. Turnover rate and reaction orders for the complete oxidation of methane on a palladium foil in excess dioxygen. *J. Catal.* **2001**, *199* (2), 291−301.
(30) Khivantsev, K.; Jaegers, N. R.; Kovarik, L.; Hanson, J. C.; Tao, F.; Tang, Y.; Zhang, X. Y.; Koleva, I. Z.; Aleksandrov, H. A.; Vayssilov, G. N.; Wang, Y.; Gao, F.; Szanyi, J. Achieving Atomic Dispersion of Highly Loaded Transition Metals in Small-Pore Zeolite SSZ-13: High-Capacity and High-Efficiency Low-Temperature CO and Passive NOx Adsorbers. *Angew. Chem., Int. Ed.* **2018**, *57* (51), 16672−16677.
(31) Khivantsev, K.; Jaegers, N. R.; Koleva, I. Z.; Aleksandrov, H. A.; Kovarik, L.; Engelhard, M.; Gao, F.; Wang, Y.; Vayssilov, G. N.; Szanyi, J. Stabilization of Super Electrophilic Pd+2 Cations in Small-Pore SSZ-13 Zeolite. *J. Phys. Chem. C* **2020**, *124* (1), 309−321.
(32) Perea, D. E.; Arslan, I.; Liu, J.; Ristanovic, Z.; Kovarik, L.; Arey, B. W.; Lercher, J. A.; Bare, S. R.; Weckhuysen, B. M. Determining the location and nearest neighbours of aluminium in zeolites with atom probe tomography. *Nat. Commun.* **2015**, *6*, 6.
(33) Devaraj, A.; Gu, M.; Colby, R.; Yan, P.; Wang, C. M.; Zheng, J. M.; Xiao, J.; Genc, A.; Zhang, J. G.; Belharouak, I.; Wang, D.; Amine, K.; Thevuthasan, S. Visualizing nanoscale 3D compositional fluctuation of lithium in advanced lithium-ion battery cathodes. *Nat. Commun.* **2015**, 6.
(34) Devaraj, A.; Vijayakumar, M.; Bao, J.; Guo, M. F.; Derewinski, M. A.; Xu, Z. J.; Gray, M. J.; Prodinger, S.; Ramasamy, K. K. Discerning the Location and Nature of Coke Deposition from Surface to Bulk of Spent Zeolite Catalysts. *Sci. Rep.* **2016**, *6*, 6.
(35) Beale, A. M.; Gao, F.; Lezcano-Gonzalez, I.; Peden, C. H. F.; Szanyi, J. Recent advances in automotive catalysis for NOx emission control by small-pore microporous materials. *Chem. Soc. Rev.* **2015**, *44* (20), 7371−7405.
(36) Gao, F.; Washton, N. M.; Wang, Y. L.; Kollar, M.; Szanyi, J.; Peden, C. H. F. Effects of Si/Al ratio on Cu/SSZ-13 NH3-SCR catalysts: Implications for the active Cu species and the roles of Bronsted acidity. *J. Catal.* **2015**, *331*, 25−38.
(37) Aylor, A. W.; Lobree, L. J.; Reimer, J. A.; Bell, A. T. Investigations of the dispersion of Pd in H-ZSM-5. *J. Catal.* **1997**, *172* (2), 453−462.
(38) Okumura, K.; Niwa, M. Regulation of the dispersion of PdO through the interaction with acid sites of zeolite studied by extended X-ray absorption fine structure. *J. Phys. Chem. B* **2000**, *104* (41), 9670−9675.
(39) Okumura, K.; Amano, J.; Yasunobu, N.; Niwa, M. X-ray absorption fine structure study of the formation of the highly dispersed PdO over ZSM-5 and the structural change of Pd induced by adsorption of NO. *J. Phys. Chem. B* **2000**, *104* (5), 1050−1057.
(40) Ali, A.; Alvarez, W.; Loughran, C. J.; Resasco, D. E. State of Pd on H-ZSM-5 and other acidic supports during the selective reduction of NO by CH4 studied by EXAFS/XANES. *Appl. Catal., B* **1997**, *14* (1−2), 13−22.
(41) Mei, D. H.; Gao, F.; Szanyi, J.; Wang, Y. Mechanistic insight into the passive NOx adsorption in the highly dispersed Pd/HBEA zeolite. *Appl. Catal., A* **2019**, *569*, 181−189.
(42) Mandal, K.; Gu, Y.; Westendorff, K. S.; Li, S.; Pihl, J. A.; Grabow, L. C.; Epling, W. S.; Paolucci, C. Condition-Dependent Pd Speciation and NO Adsorption in Pd/Zeolites. *ACS Catal.* **2020**, *10* (21), 12801−12818.
(43) McEwen, J. S.; Anggara, T.; Schneider, W. F.; Kispersky, V. F.; Miller, J. T.; Delgass, W. N.; Ribeiro, F. H. Integrated operando X-ray absorption and DFT characterization of Cu-SSZ-13 exchange sites during the selective catalytic reduction of NOx with NH3. *Catal. Today* **2012**, *184* (1), 129−144.
(44) Paolucci, C.; Khurana, I.; Parekh, A. A.; Li, S. C.; Shih, A. J.; Li, H.; Di Iorio, J. R.; Albarracin-Caballero, J. D.; Yezerets, A.; Miller, J. T.; Delgass, W. N.; Ribeiro, F. H.; Schneider, W. F.; Gounder, R. Dynamic multinuclear sites formed by mobilized copper ions in NOx selective catalytic reduction. *Science* **2017**, *357* (6354), 898−903.
(45) Adelman, B. J.; Sachtler, W. M. H. The effect of zeolitic protons on NOx reduction over Pd/ZSM-5 catalysts. *Appl. Catal., B* **1997**, *14* (1−2), 1−11.
(46) Benson, J. E.; Hwang, H. S.; Boudart, M. Hydrogen-Oxygen Titration Method for Measurement of Supported Palladium Surface-Areas. *J. Catal.* **1973**, *30* (1), 146−153.
(47) Simplicio, L. M. T.; Brandao, S. T.; Sales, E. A.; Lietti, L.; Bozon-Verduraz, F. Methane combustion over PdO-alumina catalysts: The effect of palladium precursors. *Appl. Catal., B* **2006**, *63* (1−2), 9−14.
(48) Zhu, G. H.; Han, J. Y.; Zemlyanov, D. Y.; Ribeiro, F. H. The turnover rate for the catalytic combustion of methane over palladium is not sensitive to the structure of the catalyst. *J. Am. Chem. Soc.* **2004**, *126* (32), 9896−9897.
(49) Zhang, H. B.; Liu, G. G.; Shi, L.; Ye, J. H. Single-Atom Catalysts: Emerging Multifunctional Materials in Heterogeneous Catalysis. *Adv. Energy Mater.* **2018**, *8* (1), 1701343.
(50) Wang, A. Q.; Li, J.; Zhang, T. Heterogeneous single-atom catalysis. *Nat. Rev. Chem.* **2018**, *2* (6), 65−81.
(51) Yang, X. F.; Wang, A. Q.; Qiao, B. T.; Li, J.; Liu, J. Y.; Zhang, T. Single-Atom Catalysts: A New Frontier in Heterogeneous Catalysis. *Acc. Chem. Res.* **2013**, *46* (8), 1740−1748.
(52) Chin, Y. H.; Garcia-Dieguez, M.; Iglesia, E. Dynamics and Thermodynamics of Pd-PdO Phase Transitions: Effects of Pd Cluster Size and Kinetic Implications for Catalytic Methane Combustion. *J. Phys. Chem. C* **2016**, *120* (3), 1446−1460.
(53) Van den Bossche, M.; Gronbeck, H. Methane Oxidation over PdO(101) Revealed by First-Principles Kinetic Modeling. *J. Am. Chem. Soc.* **2015**, *137* (37), 12035−12044.
(54) Goodman, E. D.; Johnston-Peck, A. C.; Dietze, E. M.; Wrasman, C. J.; Hoffman, A. S.; Abild-Pedersen, F.; Bare, S. R.; Plessow, P. N.; Cargnello, M. Catalyst deactivation via decomposition into single atoms and the role of metal loading. *Nat. Catal* **2019**, *2* (9), 748−755.
(55) Cullis, C. F.; Trimm, D. L.; Nevell, T. G. Role of Catalyst Support in Oxidation of Methane over Palladium. *J. Chem. Soc., Faraday Trans. 1* **1972**, *68* (8), 1406.

https://doi.org/10.1021/jacsau.0c00109
JACS Au 2021, 1, 396−408

(56) Chen, C.; Yeh, Y. H.; Cargnello, M.; Murray, C. B.; Fornasiero, P.; Gorte, R. J. Methane Oxidation on Pd@ZrO2/SiAl2O3 Is Enhanced by Surface Reduction of ZrO2. *ACS Catal.* **2014**, *4* (11), 3902−3909.
(57) Wang, W. Y.; Zhou, W.; Li, W.; Xiong, X. W.; Wang, Y. H.; Cheng, K.; Kang, J. C.; Zhang, Q. H.; Wang, Y. In-situ confinement of ultrasmall palladium nanoparticles in silicalite-1 for methane combustion with excellent activity and hydrothermal stability. *Appl. Catal. B-Environ* **2020**, 276.
(58) Marberger, A.; Petrov, A. W.; Steiger, P.; Elsener, M.; Krocher, O.; Nachtegaal, M.; Ferri, D. Time-resolved copper speciation during selective catalytic reduction of NO on Cu-SSZ-13. *Nature Catalysis* **2018**, *1* (3), 221−227.

https://doi.org/10.1021/jacsau.0c00109
JACS Au 2021, 1, 396−408